



# Flow and hardening behavior in the heat-affected zone of welded ultra-high strength steels

Shahriar Afkhami<sup>1</sup> · Mohsen Amraei<sup>2</sup> · Vahid Javaheri<sup>3</sup> · Mehran Ghafouri<sup>1</sup> · Timo Björk<sup>1</sup> · Antti Salminen<sup>2</sup> · Xiao-Lin Zhao<sup>4</sup>

Received: 28 August 2023 / Accepted: 29 January 2024 / Published online: 8 February 2024  
© The Author(s) 2024

## Abstract

The applications of thermomechanically processed ultra-high strength steels (UHSS) are rapidly increasing, and welding these UHSSs seems inevitable in steel structures. However, welding heat causes unwanted microstructural transformations in the heat-affected zone (HAZ). Due to the localized nature of these changes throughout the HAZ, evaluating the true stress–strain values of these localized HAZ subzones is essential to improve the accuracy of analytical or numerical models. Hence, this study utilized experimental thermal simulations to replicate HAZ subzones of two types of UHSSs, i.e., direct-quenched S960 and quenched-and-tempered S1100, and employed tensile test in conjunction with digital image correlation to plot the true stress–strain and hardening curves of the subzones. Both UHSSs manifested similar trends but with various fluctuations in their hardening capacities throughout their HAZ subzones. Next, hardening parameters from Hollomon, Voce, and Kocks-Mecking approaches were extracted by fitting the experimental results with the semi-empirical equations. For both UHSS types, the Voce approach, on average, was more accurate in modeling the plastic deformation. Also, hardening parameters achieved via the Voce approach's fittings agreed with the parameters from Kocks-Mecking plots; this consistency pointed to the predictability of the plastic flow and hardening behavior of both UHSS types. According to the microstructural investigations, the hardening behavior of the investigated HAZ subzones depended on two types of microstructure constituents: ferritic and lath-like features. Ferritic features dominantly governed the plastic flow and hardening near the fusion line, while by getting distant from the fusion line, the lath-like features became more dominant.

**Keywords** Ultra-high strength steel · Heat-affected zone · Thermomechanical simulation · True stress–strain · Hardening behavior · Microstructural evaluation

## 1 Introduction

Thermomechanically processed ultra-high strength steels (UHSS) can achieve strength levels higher than 780 MPa while maintaining their low-alloy nature with a dominantly bainitic/martensitic microstructure [1]. Hence, these alloys

provide industrial and construction sections with an economical solution to significantly decrease material and energy consumption in fabricating reliable steel structures and components [2]. However, to benefit the most from UHSSs in such applications, these steels are typically required to be subjected to welding as an effective and common joining process in steel structures [3]. Fusion welding exposes UHSSs to high amounts of concentrated heat input (HI); consequently, a series of localized microstructures (regions) form in the vicinity of the welded joints, known as their heat-affected zone (HAZ) [4]. Each of these regions with distinct localized microstructures in the HAZ is identified as a HAZ subzone in the literature. The peak temperature and cooling rate these subzones experience through welding (based on their distance from the weld fusion line) are considered the key parameters affecting the microstructure and mechanical properties of these subzones, potentially affecting the overall

✉ Mohsen Amraei  
mohsen.amraei@utu.fi

<sup>1</sup> Laboratory of Steel Structures, LUT University,  
53850 Lappeenranta, Finland

<sup>2</sup> Department of Mechanical and Materials Engineering,  
University of Turku, 20520 Turku, Finland

<sup>3</sup> Materials and Mechanical Engineering, University of Oulu,  
90014 Oulu, Finland

<sup>4</sup> Department of Civil and Environmental Engineering, The  
Hong Kong Polytechnic University, Hong Kong, Hong Kong

mechanical performance of the HAZ area and welded joint [5]. Hence, the HAZ is commonly the most critical region of welded UHSSs, governing the overall behavior of the joint. For example, the softened HAZ, as a frequent phenomenon in welded UHSSs, is almost inevitable with degraded mechanical properties such as hardness reduction of up to 60% compared to the hardness of the base metals [6–9].

By reducing the HI and altering the cooling rate, it is possible to manipulate the microstructure of the HAZ subzones, hence achieving improved joint capacity and ductility [4]. For example, Amraei et al. [10] demonstrated that the material adjacent to a highly narrow HAZ caused by laser welding generates hydrostatic stress through constraint boundary conditions, prohibiting the HAZ from deteriorating the strength and ductility of the welded joint. Therefore, in [10], despite observing a 25% reduction in the hardness values in the softened HAZ subzone of the direct-quenched S960 UHSS, the overall joint strength and ductility were improved due to this phenomenon. However, sophisticated welding processes with more accurately controlled HI, such as laser or electron beam welding, are not always available or useable, especially in field or workshop applications. Therefore, the importance of more commonly used welding processes, such as gas metal arc welding (GMAW), in joining UHSSs cannot be neglected [11]. Among various fusion welding methods, GMAW has been prominently used for welding UHSSs due to its versatile and adaptive nature, especially since the HI can be significantly manipulated via optimization and manipulation of the arc voltage, current, and shielding gas composition. Hence, it is possible via GMAW to decrease the adverse effects of fusion welding while maintaining the accessibility and applicability of the welding procedure and a high production rate [9, 12].

The literature on welded UHSSs has primarily focused on the weldments' overall performance since experimental investigation of the mechanical characteristics for distinct HAZ subzones is not feasible with acceptable accuracy and reliability via commonly available mechanical tests [13, 14]. To overcome such drawbacks, in studies such as [15, 16], and [17], the mechanical behaviors of HAZ subzones are compared mainly per the empirical correlations between the Vickers hardness values of steels and their strength or impact toughness. However, these correlations are limited to calculating the yield and ultimate strength of steels and cannot compare, for example, the whole deformation route or hardening of HAZ subzones. Further, the reliability of such correlations is not solidly established for, e.g., all HAZ subzones, and is proven not to be the same for direct-quenched and quenched-and-tempered steels since the response of each mentioned UHSS type is different due their various microstructural stability [14]. Hence, experimental approaches to locally investigate the mechanical behavior of HAZ subzones are essential to accurately evaluate, predict,

and model the mechanical performance and deformation of the weldments.

In recent years, with new measurement techniques such as digital image correlation (DIC), it has been possible to collect local strain data while testing weldments [18]. From the post-processed data, the constitutive model of the HAZ in high-strength steels has been successfully governed [19, 20]. Although these studies provide rather detailed information about the overall performance of the HAZ, they cannot provide further information on how each subzone behaves. The main limitation to extracting the stress–strain curve of each subzone is the practically limited size of those regions in actual weldments. On the other hand, a comprehensive understanding of the mechanical properties of the HAZ needs performing standard tensile tests on specimens made of each subzone coupled with DIC measurement systems. Performing such tests can provide further information on how each subzone behaves and how their interactions lead to the final joint performance [21]. However, such an approach requires test specimens subjected to thermal gradients similar to the gradients HAZ subzones experience through an actual welding procedure, and applying such gradients is currently feasible with thermomechanical simulator machines. So, utilizing a combination of thermomechanical processing, tensile test, and DIC makes experimental investigation of the actual mechanical behavior of each subzone possible.

Consequently, this study utilized a thermomechanical simulator machine to replicate various HAZ subzones of the weld HAZ for two UHSS types, i.e., direct-quenched S960 and quenched-and-tempered S1100. The HAZ subzones are replicated based on the thermal gradients during a GMAW pass typically used in steel structures, from the authors' previous research [11]. The thermally simulated subzones were then used to make tensile test specimens to plot the true stress–strain and hardening curves of each subzone. Further, the plastic deformation and hardening behavior of the simulated subzones are analyzed via semi-empirical equations proposed by Hollomon [22], Voce [23, 24], and Kocks-Mecking [25–27]. These approaches and their mathematical presentations are introduced and discussed in more detail in Section 2.4. Finally, the correlations between the microstructural features and hardening parameters, extracted from the semi-empirical approaches, are investigated using electron backscatter diffraction (EBSD) and scanning electron microscopy (SEM). The EBSD results and their analysis from the samples in this research are directly available in the authors' preceding studies in [14] and [28].

## 2 Materials and methods

Two steels, each belonging to a different type of thermomechanically processed UHSSs, are investigated in this study: direct-quenched S960 and quenched-and-tempered S1100.

These UHSSs are commonly categorized per the final stage of their thermomechanical processing, i.e., the direct-quenched ones are subjected to quenching after a thermomechanical (simultaneous) rolling and annealing procedure; in contrast, a tempering procedure follows the quenching step in quenched-and-tempered variants. The chemical compositions of these steels are presented in Table 1.

## 2.1 Numerical modeling of the thermal gradients

To simulate the thermal gradients experienced by the HAZ subzones of the studied materials, thermal cycles associated with the HAZ of a GMAW procedure having an arc voltage, welding current, speed, and linear heat input of 25 (V), 220 (A), 6.2 (mm/s), and 0.7 (kJ/mm), respectively, were numerically modeled via SmartWeld software. The outputs of the numerical models were used later as inputs for the thermal gradients applied to the samples using the Gleeble machine. The welding parameters used for the model were based on an actual GMAW butt joint, commonly used for constructional and industrial applications [11]; further details on the welding parameters and simulated thermal cycles are available in [28]. It should be noted that the validity of the simulated thermal cycles and their similarity to actual cycles experienced through the HAZ of the actual weld are approved based on the microstructural and characteristics comparisons (e.g., microhardness measurements) in [14] and [28]. Following the modeled thermal cycles and based on their distance from the fusion line, the simulated HAZ was divided into seven subzones, as presented in Table 2.

## 2.2 Gleeble thermal simulations and their subsequent metallography

After identification of the subzones per Table 1, as-received direct-quenched S960 and quenched-and-tempered S1100 ultra-high strength steels were cut from 8-mm-thick plates along their rolling direction and then machined into 55 mm × 10 mm × 5 mm blocks (seven blocks for each material to represent its seven HAZ subzones). Next, a Gleeble 3800 thermomechanical simulator was used to simulate the subzones; the thermocouples of the device were positioned in the midlength of the blocks (3-mm-long gauge area for the tensile specimens shown in Fig. 1) to accurately apply the thermal gradients presented in Table 2 to their respective specimen (machined steel block). After thermomechanical simulations, samples were labeled following their material (S960 or S1100) and the thermal gradient they experienced in the Gleeble

**Table 2** Characteristics of the simulated HAZ subzones [14, 28]

Subzone	Approximate distance from the weld fusion line	Estimated peak temperature	Estimated $\Delta t_{8/5}$
1	0.0 mm	1350 °C	10.3 s
2	0.5 mm	1154 °C	10.4 s
3	1.0 mm	1000 °C	10.5 s
4	1.5 mm	890 °C	10.7 s
5	2.0 mm	800 °C	11.6 s
6	2.5 mm	730 °C	-
7	3.0 mm	670 °C	-

machine; for example, the sample labeled as S960-1 was made of direct-quenched S960 steel and, according to Table 2, was heated up to 1350 °C and cooled down with a cooling rate that resulted in a  $\Delta t_{8/5} = 10.3$  s. Next, for microstructural analysis, the midlengths of the blocks were ground sequentially using various abrasive pads with grit numbers from 800 to 2000 and polished using 1- $\mu$ m colloidal silica to achieve a mirror-like surface. After polishing, the specimens were etched with nital for 15 s to reveal the microstructural features. Scanning electron microscopy (SEM) was then performed using a SU3500 microscope from Hi-Tech Instruments.

## 2.3 Tensile tests and the DIC technique

For quasi-static tensile tests, the blocks were machined into the dimensions shown in Fig. 1 to be used as sub-size tensile specimens. The selected dimensions were compatible with sample size limitations associated with the Gleeble thermomechanical simulator and the tensile test rig. A 150-kN in-house test rig was used to conduct the quasi-static tensile tests at room temperature (20 °C), with a constant strain rate of  $5 \times 10^{-4} \text{ s}^{-1}$  (i.e., 0.0015 mm/s). An ARAMIS digital image correlation system (developed by ZEISS, Germany) was used during the tensile tests to record the tests visually for later calculations. The ARAMIS system included a camera pair (equipped with 75-mm lenses) and a 12 M deformation sensor for image recordings with a frame rate of 5 fps; the sensor was calibrated with a working distance, camera angle, and the distance between the cameras of 410 mm, 25°, and 142 mm. This calibration setup resulted in a deviation of 0.034 pixels. The GOM correlate software (version 2019 Hotfix 7), developed by ZEISS, Germany, was used to calculate the true stress and logarithmic strain values at the necking region of the samples. The logarithmic strain

**Table 1** Chemical compositions of the base metals [14]

Material	$C_{\text{wt}\%}$	$Si_{\text{wt}\%}$	$Mn_{\text{wt}\%}$	$P_{\text{wt}\%}$	$S_{\text{wt}\%}$	$V_{\text{wt}\%}$	$Cu_{\text{wt}\%}$	$Cr_{\text{wt}\%}$	$Ni_{\text{wt}\%}$	$Mo_{\text{wt}\%}$
S960	0.088	0.040	1.130	0.010	-	0.009	0.011	1.000	0.050	0.117
S1100	0.133	0.192	1.490	0.006	0.001	0.152	0.437	1.340	0.998	0.388

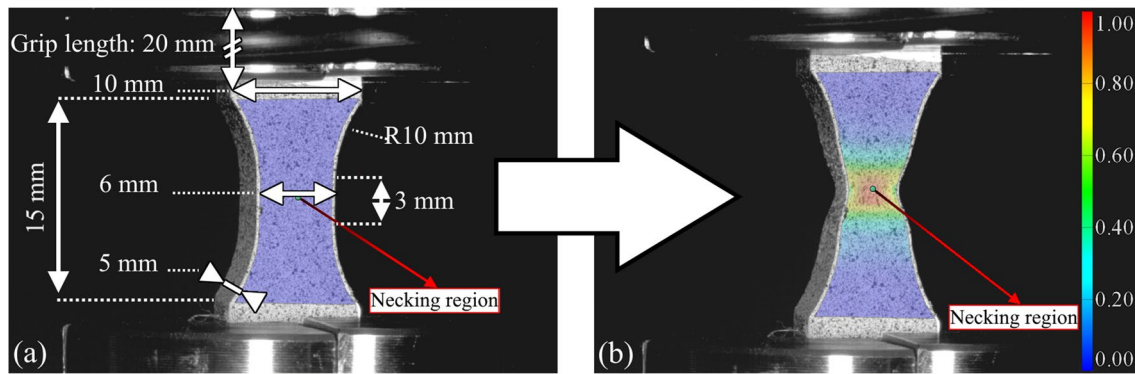


**Fig. 1** **a** Actual view of a tensile specimen, including the specimen's general dimensions, at the beginning of its tensile test. **b** The same specimen at the end of the test and before its final fracture (color

codes represent the logarithmic strain values throughout the sample; the schematic view of the specimen is available as supplementary material)

values were measured by image-by-image comparison of the speckle pattern on the samples' surface (Fig. 1). The speckle pattern was applied on the samples' surface using a commercial speckle pattern application kit from Correlated Solutions Europe (Germany). Also, the true stress values were calculated with the same software via the constant volume approach [29] using the local logarithmic strain values achieved from the DIC technique in conjunction with global external load values recorded from a load cell (test rig) and considering the material continuity as the boundary condition. It should be noted that a temporal smoothing spline filter of the degree of 30 (the data filter is available as an option in the GOM correlate software) was used for true stress and logarithmic strain data to minimize numerical errors and maximize the curves' smoothness and coherency. Also, the hardening curves were later calculated and plotted based on the first derivatives of the stress–strain curves, after applying an extra average filter on the stress–strain curves using Microsoft Excel (moving average with interval value of 10) to minimize incoherencies and omitting any extreme jerkiness from the evaluations.

## 2.4 Analytical background

The plastic deformation and hardening behavior of metals can generally be described via semi-empirical equations between

true stress and plastic strain values. For example, depending on the metal type and deformation condition, equations proposed by Ludwik [30], Hollomon [22], Swift [23], Ludwiginson [31], or Voce [24] can construe the plastic deformation from its onset (the yielding) to the point of instability (the necking). Among these equations, the Hollomon equation (Eq. 1) and the Voce equation (Eq. 2) are commonly used for carbon or low-alloy steels; the main reasons behind the popularity of these two equations for carbon and low-alloy steels are the simplicity of the former and the relatively better accuracy of the latter [32–34]:

$$\sigma = K \varepsilon_p^n \quad (1)$$

$$\sigma = \sigma_s - (\sigma_s - \sigma_l) \times \exp(n_v \times \varepsilon_p) \quad (2)$$

In these equations,  $\sigma$  is the true stress (MPa),  $\varepsilon_p$  is the true plastic strain,  $K$  is the strain hardening coefficient (MPa),  $n$  is the strain hardening exponent,  $\sigma_s$  is the saturation stress (MPa),  $\sigma_l$  is the initial true stress (MPa), and  $n_v$  is the rate parameter. Following the definition of 0.2% offset yield strength, the yielding point of the material in each specimen ( $\sigma_y$ ) was defined as the stress value where the  $\Delta$  in Eq. 3 becomes negative:

$$\Delta = (\sigma/E + 0.002) - \varepsilon \quad (3)$$

**Table 3** Calculated  $\sigma_y$  (MPa) values

Material	Subzone 1	Subzone 2	Subzone 3	Subzone 4	Subzone 5	Subzone 6	Subzone 7
S960	737	832	922	734	949	736	785
S1100	798	877	1414	1021	1296	1153	1153

**Table 4** Calculated  $\sigma_u$  (MPa) values

Material	Subzone 1	Subzone 2	Subzone 3	Subzone 4	Subzone 5	Subzone 6	Subzone 7
S960	1035	1079	1046	972	936	904	935
S1100	1447	1485	1512	1511	1352	1329	1340

where  $E$  is the tangent modulus of the subzone (extracted from the slope of the linear portion of the  $\sigma$ - $\varepsilon$  curves), and  $\varepsilon$  is the strain value corresponding to the  $\sigma$  in the linear region. Also, based on the correlation between the engineering stress and true stress values, the moment at which the necking occurs (stability limit) in the stress–strain curves was defined as the true stress value ( $\sigma_u$ ) at which the calculated engineering stress ( $S$ ) in Eq. 4 reaches its maximum:

$$S = \sigma / \exp(\varepsilon) \tag{4}$$

Also, another intrinsic hardening parameter considered for comparisons was the hardening capacity ( $H_c$ ), calculated via Eq. 5:

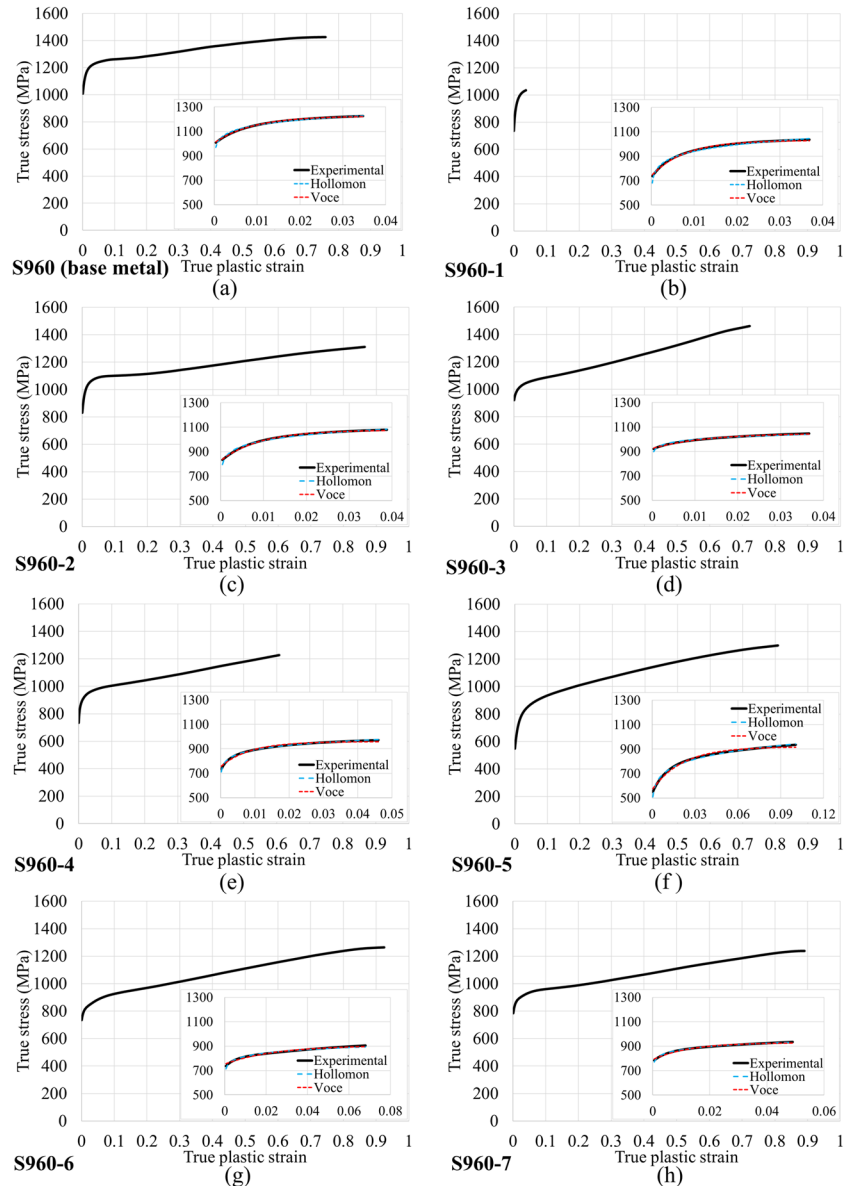
$$H_c = (\sigma_u / \sigma_y) - 1 \tag{5}$$

### 3 Results and discussion

The values of  $\sigma_y$  and  $\sigma_u$ , calculated from Eq. 3 and Eq. 4 for the HAZ subzones, are reported in Tables 3 and 4, respectively. It should be noted that the values reported in these tables are slightly different from the ones reported in [28] since the strength values in [28] were calculated from the engineering curves achieved from a 3-mm gauge length, while the values reported in this study are locally calculated for the necking region, e.g., the one marked in Fig. 1.

Accordingly, in the following subsections, the Hollomon and Voce equations are first fitted to the results of the quasi-static tensile tests to compare the suitability of these equations to model the flow behavior of HAZs of UHSSs up to their necking point and then extract the hardening

**Fig. 2 a–h** True stress–logarithmic strain curves of S960 and its simulated HAZ subzones



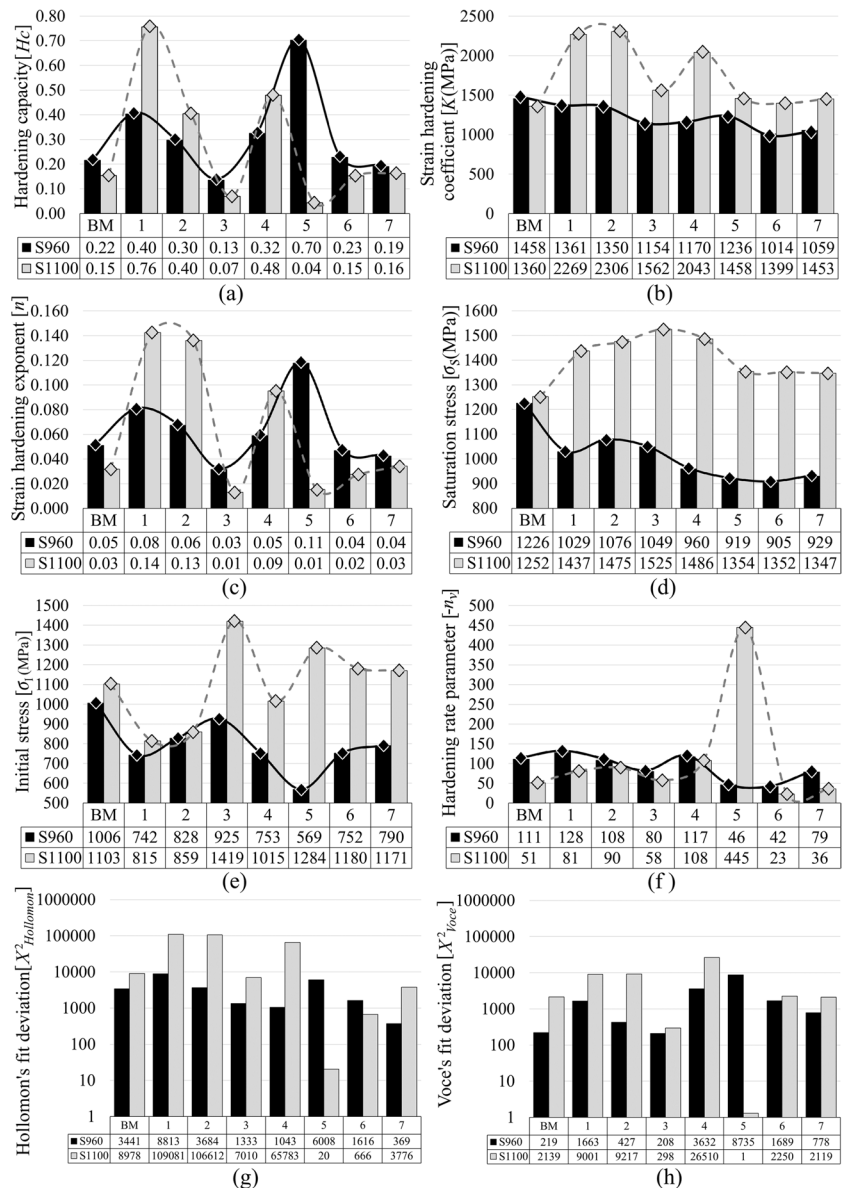
parameters of the HAZ subzones described in Table 2 for each steel to have a comparison between different subzones and also between subzones with similar thermal cycles but from different UHSSs (S960 and S1100). Ultimately, these comparisons and their associated discussions around the reasons behind the differences in the hardening parameters from the microstructural point of view further clarify governing parameters of the plastic deformation in welded quenched-and-tempered and direct-quenched UHSSs.

### 3.1 Direct-quenched S960

True stress–logarithmic strain curves of the specimens S960-1 to S960-7, besides S960’s as the base metal, are shown in Fig. 2. The elastic regions of the curves are

removed from the results since the elastic behavior of the specimens is out of the scope of this study; however, a thorough evaluation of the engineering stress–strain curves of the samples, including their elastic behavior, hardness, and other typical mechanical properties, is available in [28]. The best fits of the Hollomon and Voce equations for each subzone, from their yielding to the necking point, are also shown as insets in Fig. 2. According to these figures, the plastic deformation and flow behavior of the S960 significantly changed per its distance from the fusion line. From the curves and fits in Fig. 2, the hardening parameters are extracted and visually presented in Fig. 3 for better comparison. According to Fig. 3, compared to the base metal,  $H_c$  increased at S960-1 and gradually decreased until subzone 3; then, there was a significant increase in  $H_c$  at zones 4 and 5.

**Fig. 3** a–h Parametric comparisons of the hardening parameters for S960, S1100, and their simulated HAZ subzones

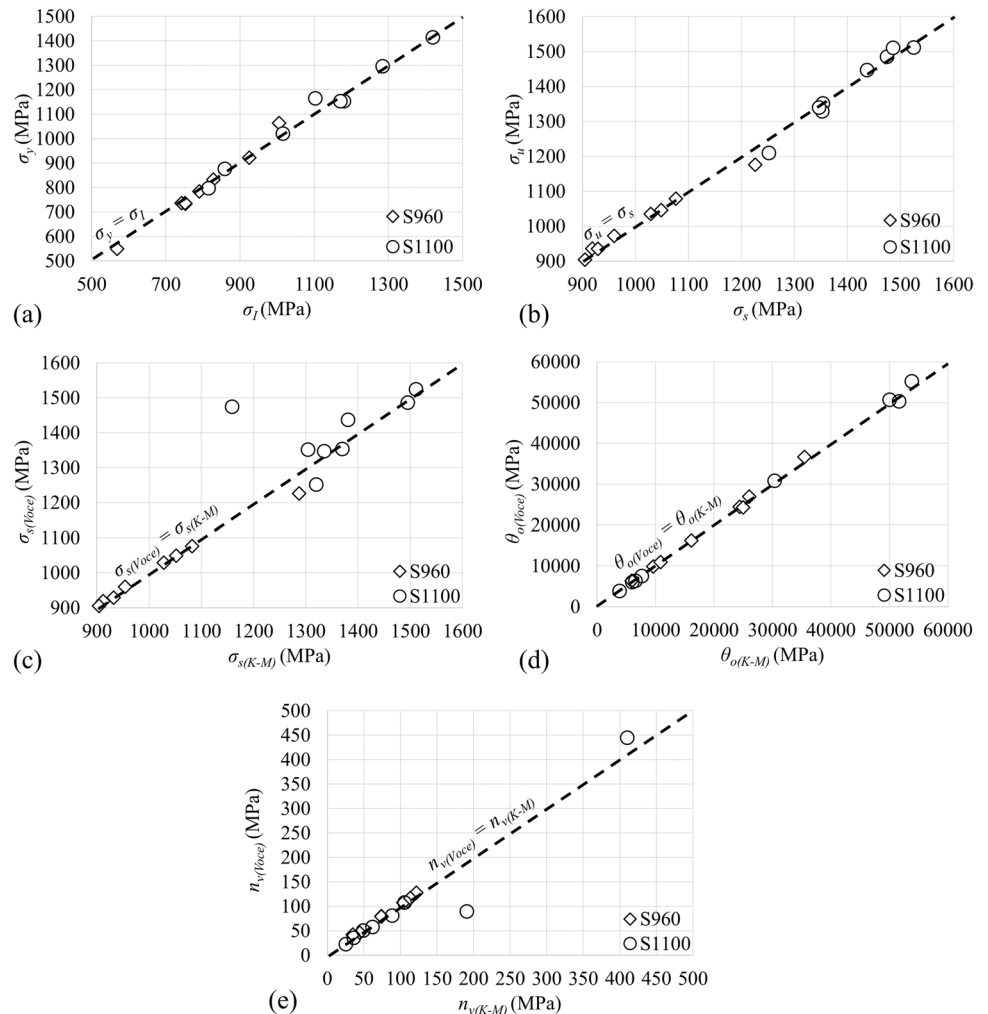


Finally, the  $H_c$  was similar to the base metal in zones 6 and 7. Regarding the Hollomon parameters, according to Fig. 3,  $n$  had a similar trend as  $H_c$ , confirming  $n$  as the governing parameter in the Hollomon equation to describe the hardening behavior of S960 and its HAZ subzones. It should be noted that although  $K$  also changed per distance from the fusion line, the fluctuation domain of  $K$ , as a coefficient, was negligible ( $1000 \text{ MPa} < \approx K < 1450 \text{ MPa}$ ) compared to  $n$ , as the exponent, and  $K$  did not show a clear trend even in this limited domain of changes.

The effect of distance from the fusion line on the Voce parameters can also be seen in Fig. 3. Regarding the Voce parameters, ideally in metals, the  $\sigma_i$  and  $\sigma_s$  parameters must have the same values as  $\sigma_y$  and  $\sigma_u$ , respectively. As shown in Fig. 4, the Voce equation successfully estimated the strength values of the HAZ subzones for S960 with significant accuracy, making the flow deformation of S960 through its HAZ subzones quite predictable using Voce’s approach. To evaluate the instantaneous hardening behavior of the specimens, following the Kocks-Mecking (K-M) approach, the strain hardening rates ( $\theta = d\sigma / d\epsilon_p$ ) of the specimens

are plotted against their corresponding flow stress ( $\sigma - \sigma_y$ ) values (Fig. 5) and  $\epsilon_p$  (Fig. 5’s insets). The K-M plots can be utilized as a complementary method accompanying the Voce approach to evaluate its validity in analyzing the hardening behavior of metals. The Voce equation views the flow curve of metals as a transition of state between an initial flow stress ( $\sigma_i$ ) and a saturation stress ( $\sigma_s$ ), indicating an equilibrium state at any given strain rate and temperature [35, 36], while  $\sigma_i$ ,  $\sigma_s$ , and  $n_v$ , as Voce’s parameters, can also be extracted from K-M plots; consistency between the parameter values achieved from the Voce and K-M methods can indicate the predictability of the material’s behavior [37]. Also, prominent changes in K-M plots can reveal microstructural evolutions during deformation [38]. In Fig. 5, the necking point as the stability limit of the material is marked with a green dashed line in each curve. According to the K-M approach, the strain hardening rate-flow stress curve can be divided into different regions based on the strain hardening rate’s drop order. The sharp drop in the  $\theta$  values at low flow stresses is called stage I strain hardening, which is followed by a linear decrease known as stage II, and eventually, it

**Fig. 4 a–e** Comparisons between the Voce parameters, strength values, and K-M parameters



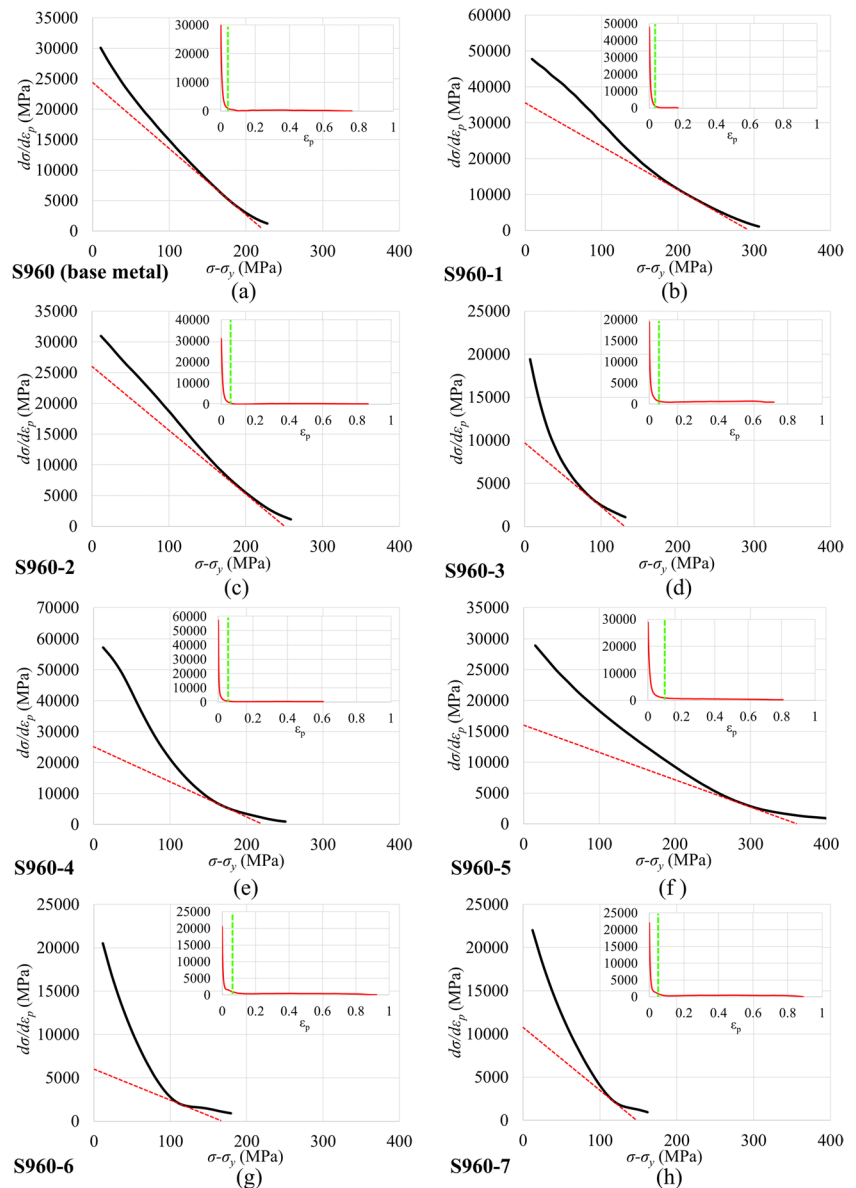
is followed by a gradual decrease at relatively higher flow stress values. The gradual decrease of  $\theta$  at relatively higher flow stress values is known as stage III hardening and can be typically marked by a change in the curvature of the graph at the end of its sudden drop (stage I), should the material have not a clear linear hardening stage (stage II) [33].

The importance of stage III hardening stems from its significant sensitivity to deformation rate and temperature [25], making it possible to calculate parameters such as  $\sigma_f$ ,  $\sigma_s$ , and  $n_v$  using the tangent line along stage III in K-M graphs. The tangent line is marked as a red dashed line in Fig. 5. Accordingly, the intercept of the tangent line with the ordinate in the K-M curves marks the initial strain hardening rate ( $\theta_o$ ) of the specimens;  $\theta_o$  can also be calculated as  $n_v \times (\sigma_f - \sigma_s)$  using the Voce approach. Also, the intercept with the abscissa indicates the flow stress at the onset of plastic flow, which

ideally equals  $\sigma_s - \sigma_y$ . Finally, the slope of the tangent line should equal the  $n_v$  value. Therefore, it is possible to calculate  $\theta_o$ ,  $n_v$ , and  $\sigma_s$  via both the K-M and Voce approaches; consistency between the results of these methods can be attributed to the flow behavior's predictability. As shown in Fig. 4, for S960 and all its HAZ subzones, there is a good agreement between the parameters calculated via the K-M method and those achieved from the Voce equation.

Microstructural features of the S960 specimens are available in Fig. 6. From the microstructural point of view, cubic metals' plastic deformation is typically governed by dislocations (their nucleation, annihilation, and interactions) and different microstructural obstacles (such as precipitates and various boundaries) hindering dislocation movement. Further, dislocation pile-up or accumulation is the dominant hardening mechanism in such metals [34, 39]. Different

**Fig. 5** a–h Kocks-Mecking curves of S960 and its HAZ subzones



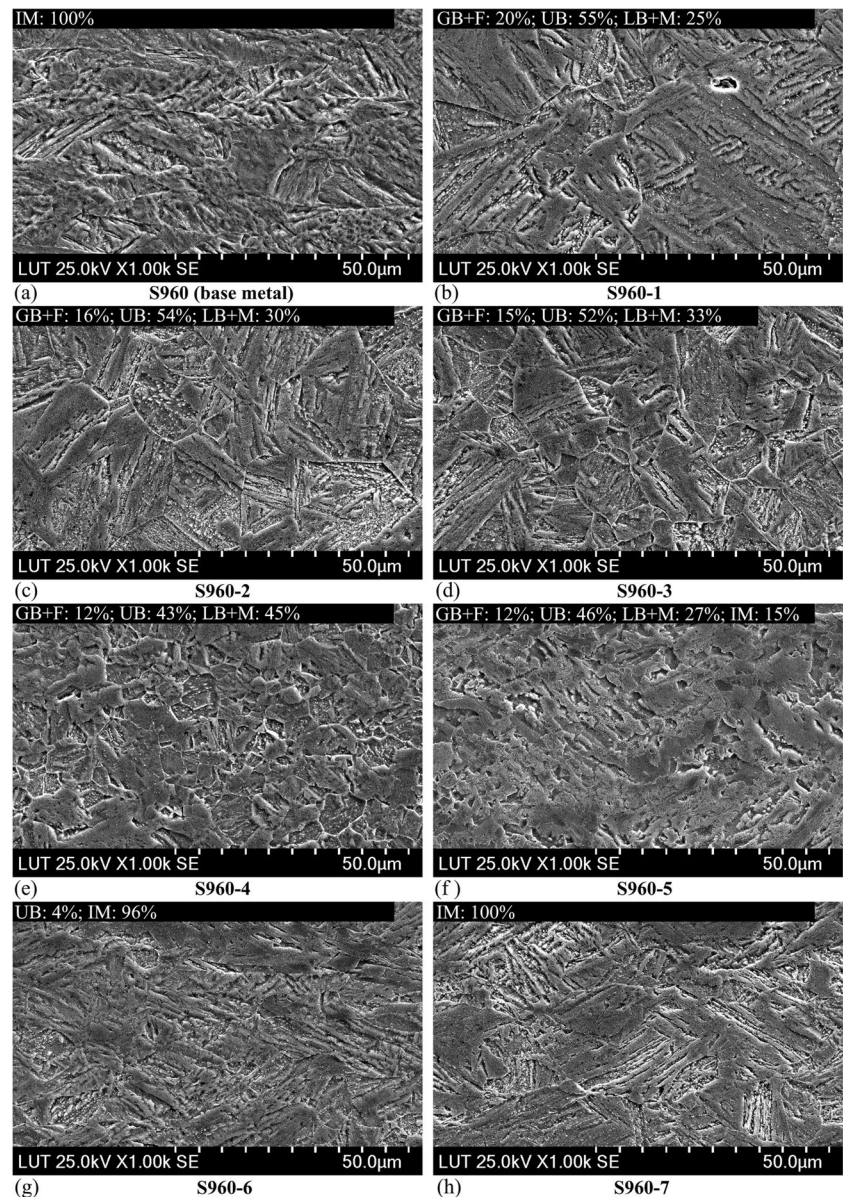


phase constituents and their size and fractions in each sample must be considered to establish a correlation between the microstructural features and the flow and hardening behavior of S960 through its HAZ subzones. Considering the CCT diagram of S960 in [14], specimens S960-1 to S960-4 experienced full austenitization at their peak temperature and transformed into a mixture of ferritic features, bainite, and martensite during the cooling down to room temperature. Also, compared to the base metal, the textured microstructure caused by the fabrication procedure of the base metal (features being elongated along the rolling direction) was diminished in fully austenitized subzones. Finally, there was a significant increase in the prior austenite grain size (PAGS) due to the highest peak temperature experienced by S960-1 (further detail on microstructural evaluations of

specimens used in this research can be found in [14]). The summation of all these factors causes a complex correlation between the flow behavior of the S960 HAZ subzones and their microstructures.

Accordingly, the microstructural constituents of the S960 subzones can be divided into two groups based on their nature and following the image quality (IQ) analysis from the EBSD data of the specimens used in this study, available in [14]: first, martensite (M) and lower bainite (LB) with lath-like substructures and high microstructural strains, and second, ferrite (F), granular bainite (GB), and upper bainite (UB) with more ferritic characteristics. The fraction of each microstructural constituent, besides the untransformed initial microstructure (IM), is also presented in Fig. 6. In the first group, due to their fine-sized microstructures, the dominant

**Fig. 6** a–h Microstructural features of S960 and its HAZ subzones (initial microstructure (IM), martensite (M), lower bainite (LB), ferrite (F), granular bainite (GB), and upper bainite (UB))



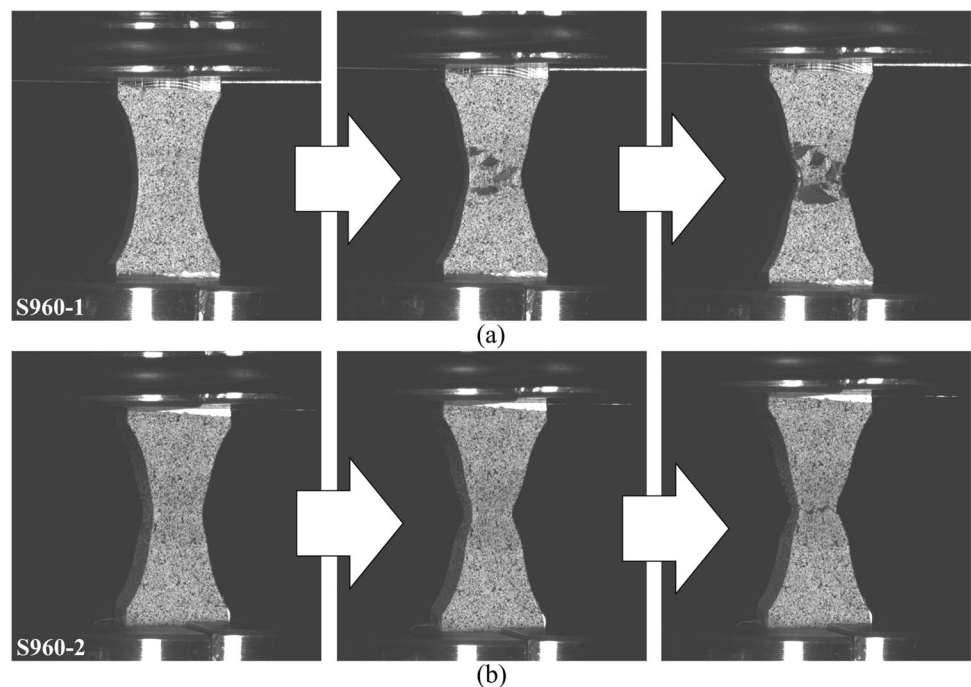
deformation mechanism is sliding of boundaries with misorientations ranging from  $5^\circ$  to  $15^\circ$ , more likely contributing to lath-like features in such microstructures. Any increase in the overall length of such boundaries (and the amount of their related phase constituents, i.e., martensite and lower bainite) increases the hardening capacity of the material due to higher dislocation densities and pinning effect associated with such microstructural features [40, 41]. However, in the features defined via high-angle grain boundaries (HAGB), i.e., features with more ferritic natures, the hardening capacity depends on the microstructure's morphological texture and grain size [42]. In such features, having a larger average grain size or PAGES with more granular-shaped morphologies decreases the strength per the Hall–Petch mechanism, increases the dislocation storage capacity of the grains, and maximizes the difference in the material flow resistance along the HAGBs and their interior microstructures. Hence, in the second group of microstructural constituents, any decrease in the average grain size can decrease the hardening capacity of metals [42–44].

According to Fig. 6, significantly higher average PAGES and disappearance of fibrous elongated morphological texture contributed to the sudden increase in the  $H_c$  (and, subsequently,  $n$ ) in S960-1, compared to the base metal [34]. There was no significant change in the phase ratios from S960-1 to S960-3; hence, the contribution of the lath-like features in these regions remained the same. However, the average PAGES decreased gradually from S960-1 to S960-3, following the contribution of the second-type microstructural constituent, potentially causing  $H_c$  to decrease until reaching its minimum in S960-3 (further detail on microstructural evaluations of specimens used in this research

with their EBSD results can be found in [14]). Next, there was an increase in  $H_c$  and  $n$  from S960-3 to S960-4, possibly due to increased lath-like features up to 45% [14], as shown in Fig. 6. The hardening capacity continued to increase from S960-4 to S960-5. Unlike its predecessors, S960-5 experienced partial austenitization and relatively lower cooling rates, eventually resulting in most of its microstructure being a mixture of ferritic features caused by tempering of the initial microstructure or slow cooling of the partially austenitized one, a combination of lower bainite and martensite, and some untransformed initial microstructure. From the IQ analysis in [14], the summation of lath-like feature in S960-5 can be estimated at 43% (untransformed initial microstructure + lower bainite / martensite), and the remaining ferritic features (upper bainite + ferrite + granular bainite) had a relatively small average grain size. Hence, the combination of these microstructural constituents favored the hardening capacity and caused an increase in  $H_c$  in S960-5. For S960-6 and S960-7, as shown in Fig. 6, the peak temperature was not high enough to trigger austenitization; also, the elongated morphological texture from the base metal was not significantly altered. Hence, these zones comprised mainly the untransformed base metal microstructure [14], which caused the  $H_c$  of these regions to be similar to the base metal. Although their strength level was lower than S960's (due to the tempered features), the simultaneous drop in their  $\sigma_y$  and  $\sigma_u$  values maintained their  $H_c$  [10, 14, 28].

According to the insets in Fig. 5 (the K-M plots), there was a minor recovery stage in the hardening of the base metal and its HAZ subzones after their necking point, which potentially contributed to the relatively high elongation at

**Fig. 7** Deformation sequence of **a** S960-1 and **b** S960-2 from the onset of their necking to their final rupture



failure (final  $\epsilon_p$ ) of S960 and its HAZ subzones [42]. Considering trace amounts of retained austenite being detected in the base metal and all its HAZ subzones (white spots along the HAGBs) [14], the recovery stage can be attributed to the retained austenite and its subsequent strain-induced transformation to martensite, triggered at high deformation values beyond the stability limit of the material [41]. In this regard, S960-1 in Fig. 5 was considered an exception and was excluded from this deduction since this sample, unlike others, failed from a widespread microvoid coalescence throughout the whole gauge area, causing a possible premature rupture after the necking, as shown in Fig. 7. The extremely high peak temperature of S960-1 possibly affected regions beyond the gauge area, instead of just the midsection and ultimately caused this fracture mechanism in S960-1.

### 3.2 Quenched-and-tempered S1100

True stress–logarithmic strain curves (with their best Hollomon and Voce fits) of quenched-and-tempered S1100 are presented in Fig. 8; also, the K-M plots are shown in Fig. 9 while the microstructural features of S1100 (as the base metal) and its HAZ subzones are presented in Fig. 10. It should be noted that due to technical difficulties, some grip sliding occurred during the tensile test of S1100-5, and consequently, its results were excluded from the discussions here; however, S960-5’s data were included in the results for coherency. Also, following the patterns in Fig. 3, microstructural analysis from Fig. 10, and EBSD data available in [14], the  $H_c$  of S1100 is expected to continue increasing from S1100-4 to S1100-5, although it is not the case for the actual results in

**Fig. 8 a–h** True stress–logarithmic strain curves of S1100 and its simulated HAZ subzones

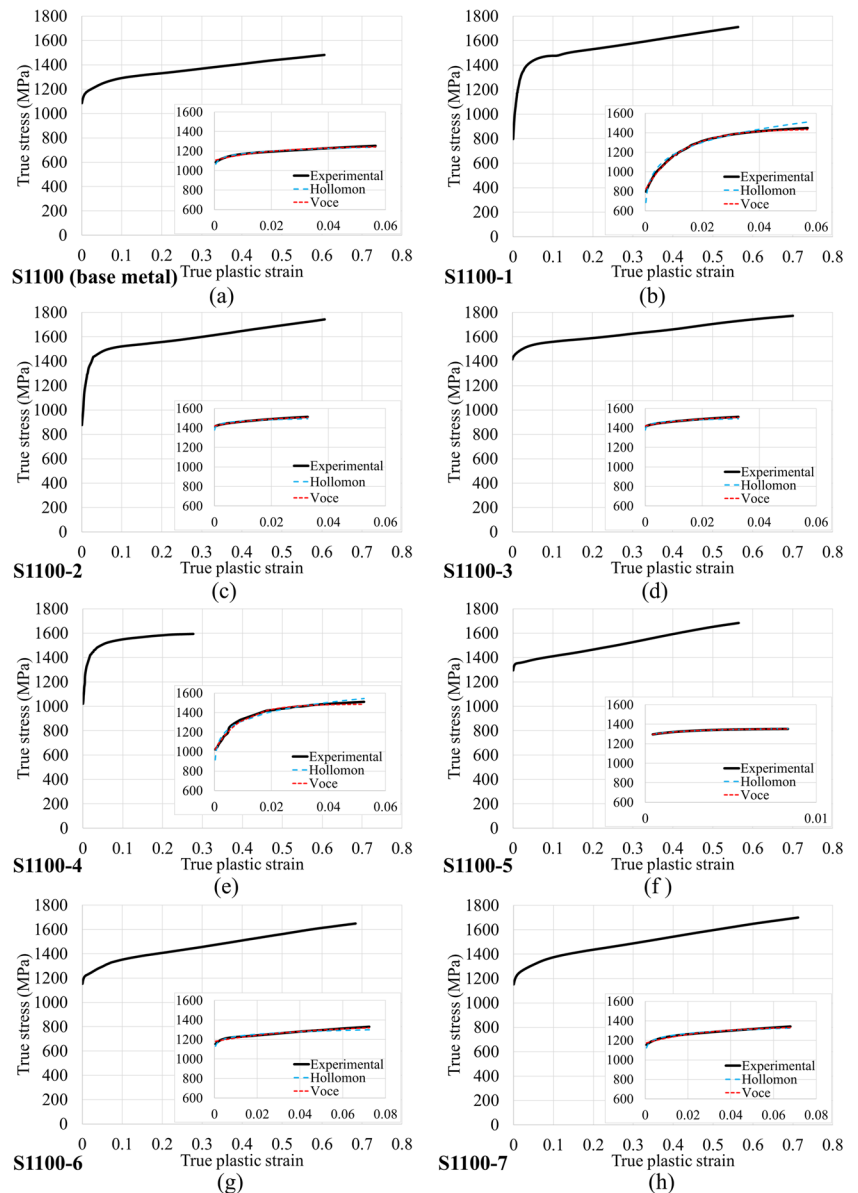


**Fig. 9** a–h Kocks-Mecking curves of S1100 and its HAZ subzones

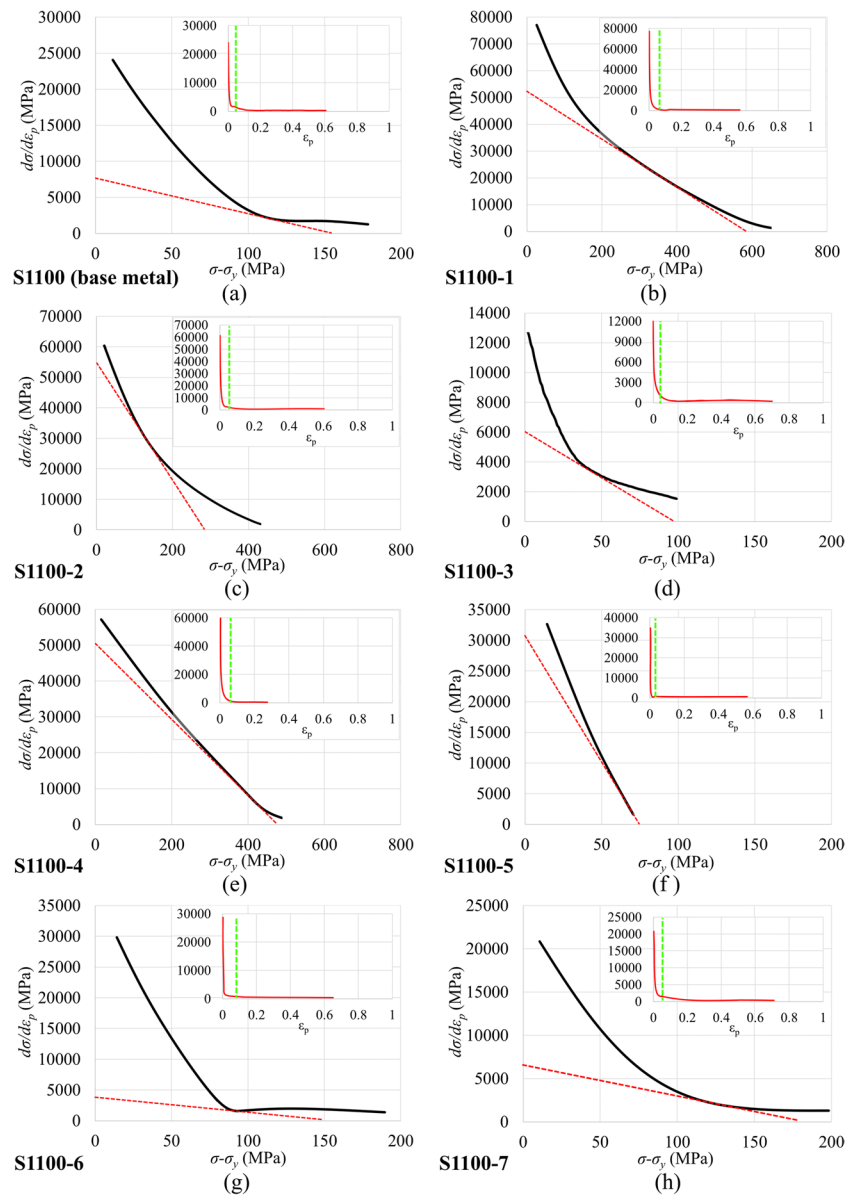
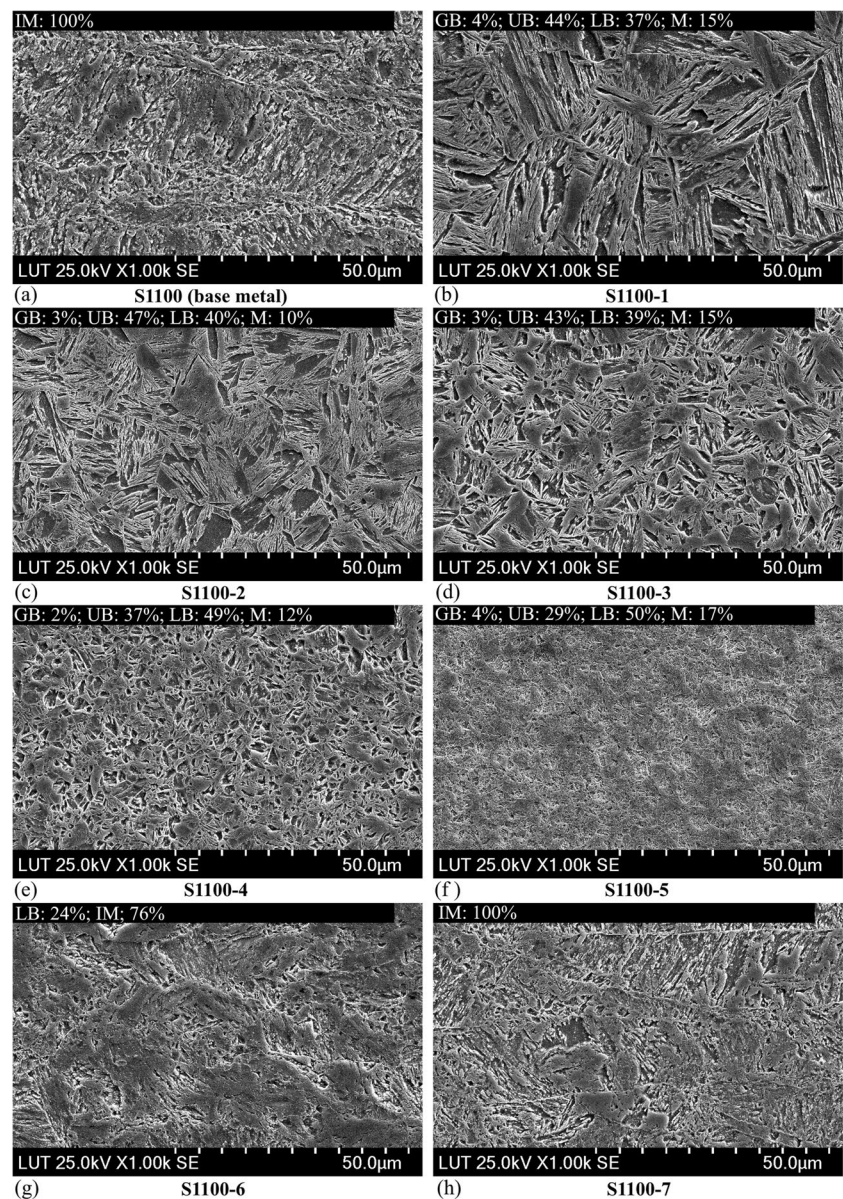


Fig. 3 due to the grip sliding occurred during the tensile test of S1100-5. Following this consideration and according to Fig. 3, the  $H_c$  of S1100, as a thermomechanically processed quenched-and-tempered steel, showed a similar pattern to that of the direct-quenched S960. Compared to S960, S1100 had a lower A3 temperature (783 °C compared to 826 °C), resulting in subzones S1100-1 to S1100-5 being fully austenitized during their heating stage [14]. Similar to S960, the elongated morphological texture was omitted from these regions, and there was a significant size increase in the PAGS in S1100-1, which was followed by a gradual decrease until S1100-5 [14]. Also, according to the IQ analysis in [14] and as shown in Fig. 10, there was a relative balance ( $\approx 50\text{--}50\%$ ) between the lath-like (martensite + lower bainite) and ferritic (granular and upper bainite) in S1100-1, S1100-2, and S1100-3. Hence,

it seems that the average of PAGS governed the  $H_c$  in these regions since the overall ratio of the characteristic constituent did not differ significantly in these samples, but the PAGS decreased from S1100-1 to S1100-3, and the  $H_c$  also gradually decreased. However, the balance was noticeably changed in S1100-4 in favor of lath-like features, assumably causing the significant  $H_c$  increase in S1100-4 shown in Fig. 3. This increase is expected to progress further in S1100-5, although it is not the case in Fig. 3; as mentioned, due to the grip sliding, S1100-5's results are excluded from this discussion as test errors in Figs. 3 and 4. Finally, the reappearance of untransformed microstructural features [14] caused the  $H_c$  in S1100-6 and S1100-7 to be similar to the base metal.

Following the K-M graphs of the S1100 specimens in Fig. 9, there was a noticeable consistency between the

**Fig. 10 a–h** Microstructural features of S1100 and its HAZ subzones (initial microstructure (IM), martensite (M), lower bainite (LB), ferrite (F), granular bainite (GB), and upper bainite (UB))



parameters extracted via the K-M plots and those from the Voce equation, as shown in Fig. 4. However, S1100-2 did not show such a significant consistency in Fig. 4, and the saturation stress and the rate parameter were under- and overestimated, respectively, using the K-M plots. Considering the sub-size dimensions of the samples, the ultra-high strength levels of S1100, and the average filter applied on the  $\theta$ - $(\sigma-\sigma_y)$  curves in Fig. 9, such a discrepancy in one sample can be considered an inevitable error caused by the test setup or statistical analysis. Hence, in general, it seems safe to conclude that the trends shown in Fig. 4 for S1100 and its HAZ subzones indicate the predictability of its flow behavior. Also, according to the insets of Fig. 9, the hardening recovery stage was present for the S1100 specimens after their instability point, especially for the

fully austenitized samples with higher peak temperatures (S1100-1, S1100-2, and S1100-3). This behavior speculated the dominant role of retained austenite in the recovery stage in ultra-high strength steels, regardless of their direct-quenched or quenched-and-tempered nature. Finally, based on the deviation square-root ( $X^2$ ) values of the Voce and Hollomon fits in Fig. 3 for both the S960's and the S1100's samples, the Voce approach showed better accuracy in predicting the flow behavior of thermomechanically processed ultra-high strength steels, regardless of their type. According to Figs. 2 and 8, most of the inaccuracies from the Hollomon approach occurred at the beginning of the plastic deformations or close to the instability point (deformations with the minimum and maximum plastic deformations before necking, accordingly).

## 4 Conclusions

In this study, HAZ subzones of two different ultra-high strength steels (direct-quenched S960 and quenched-and-tempered S1100) were thermally simulated using a Gleeble 3800 device and compared from the flow behavior, plastic deformation, and hardening perspectives. Furthermore, the correlations between the microstructural features and hardening trends were investigated using SEM images available in the current study and the relevant EBSD and IQ data from the predecessor research available in [14] and [28]. Consequently, the following points were made as concluding remarks:

- Both direct-quenched S960 and quenched-and-tempered S1100 showed similar trends in their  $H_c$ . This similarity can be attributed to similar trends in the dislocation hardening and annihilation of these steels just beyond their elastic deformation up to their necking point.
- There was an agreement between the  $H_c$  and  $n$  in both ultra-high strength steel types, proving  $n$  to be the dominant factor determining the hardening behavior of the materials in the Hollomon approach. This agreement between  $H_c$  and  $n$  also points to the potential roles of dislocation hardening and annihilation, in microstructural scales, upon  $n$  fluctuations, considering the dependency of  $H_c$  on dislocation hardening and annihilation.
- There was an agreement between the  $\sigma_I$  and  $\sigma_s$ , as Voce parameters, and  $\sigma_y$  and  $\sigma_u$ , as material properties, confirming the acceptable predictability of the flow behavior of S960 and S1100 via the Voce approach throughout their HAZ subzones.
- The S960 and S1100 subzones' microstructural constituents can be divided into two groups of lath-like and ferritic features per their nature. Constituents of each group contributed to the hardening and deformation mechanisms of the materials differently. In the regions where the ferritic features were dominant upon the hardening (especially fully austenitized regions, such as S960-1 and S1100-1), the average PAGS was deemed the most influential factor. In contrast, martensite and lower bainite contents had the determining role in other subzones (especially the partially austenitized ones).

Finally, this study highlights the main microstructural contributors to the plastic deformation and hardening of the HAZ in UHSSs to clarify the plastic deformation of the weldments made of these alloys. Such evaluations are essential to make, for example, the analytical and finite element models of such components more accurate and realistic, especially when simulating the material behavior beyond its elastic limit up to its final failure. Also, results and discussions associated with this research can be used to evaluate the plastic field and hardening behavior adjacent to external factors, e.g., cold cracks caused by

hydrogen embrittlement [42, 45, 46]. Furthermore, according to this research, compared to Hollomon, the Voce approach can be considered a more accurate and comprehensive approach for predicting the flow behavior of the ultra-high strength steels, considering its relatively lower  $X^2$  values than the Hollomon method and its significant consistency with the K-M method.

**Supplementary Information** The online version contains supplementary material available at <https://doi.org/10.1007/s40194-024-01703-x>.

**Acknowledgements** Shahriar Afkhami would like to acknowledge the financial support provided by the FOSSA project and thank all the project partners. Vahid Javaheri would like to thank Jane ja Aatos Erkon säätiö (JAES) and Tiina ja Antti Herlinin säätiö (TAHS) for their financial support on the Advanced Steels for Green Planet project.

**Funding** Open Access funding provided by University of Turku (including Turku University Central Hospital).

## Declarations

**Competing interests** The authors declare no competing interests.

**Open Access** This article is licensed under a Creative Commons Attribution 4.0 International License, which permits use, sharing, adaptation, distribution and reproduction in any medium or format, as long as you give appropriate credit to the original author(s) and the source, provide a link to the Creative Commons licence, and indicate if changes were made. The images or other third party material in this article are included in the article's Creative Commons licence, unless indicated otherwise in a credit line to the material. If material is not included in the article's Creative Commons licence and your intended use is not permitted by statutory regulation or exceeds the permitted use, you will need to obtain permission directly from the copyright holder. To view a copy of this licence, visit <http://creativecommons.org/licenses/by/4.0/>.

## References

1. Keeler S, Kimchi M, Mooney PJ (2017) Advanced high-strength steels application guidelines. World Auto Steel. [Accessed 26.12.2023] via: <https://www.worldautosteel.org/>
2. Keränen L, Kangaspuoskari M, Niskanen J (2021) Ultrahigh-strength steels at elevated temperatures. J Constr Steel Res 183:106739. <https://doi.org/10.1016/J.JCSR.2021.106739>
3. Shome M, Tumuluru M (2015) Introduction to welding and joining of advanced high-strength steels (AHSS). Welding and joining of advanced high strength steels (AHSS). Elsevier, pp 1–8
4. Amraei M, Ahola A, Afkhami S et al (2019) Effects of heat input on the mechanical properties of butt-welded high and ultra-high strength steels. Eng Struct 198:109460. <https://doi.org/10.1016/j.engstruct.2019.109460>
5. Porter DA (2015) Weldable high-strength steels : challenges and engineering applications. In: Proceedings of the IIW International conference high-strength materials-challenges and applications. Helsinki, Finland
6. Farrokhi F, Siltanen J, Salminen A (2015) Fiber laser welding of direct-quenched ultrahigh strength steels: evaluation of hardness, tensile strength, and toughness properties at subzero temperatures. J Manuf Sci Eng Trans ASME 137:061012. <https://doi.org/10.1115/1.4030177>

7. Jiao H, Zhao XL, Lau A (2015) Hardness and compressive capacity of longitudinally welded very high strength steel tubes. *J Constr Steel Res* 114:405–416. <https://doi.org/10.1016/j.jcsr.2015.09.008>
8. Pramanick AK, Das H, Lee JW et al (2021) Texture analysis and joint performance of laser-welded similar and dissimilar dual-phase and complex-phase ultra-high-strength steels. *Mater Charact* 174:111035. <https://doi.org/10.1016/j.matchar.2021.111035>
9. Brabec J, Ježek Š, Beneš L et al (2021) Suitability confirmation for welding ultra-high strength steel S1100QL using the RapidWeld method. *Manuf Technol* 21:29–36. <https://doi.org/10.21062/mft.2021.014>
10. Amraei M, Skriko T, Björk T, Zhao XL (2016) Plastic strain characteristics of butt-welded ultra-high strength steel (UHSS). *Thin-Walled Struct* 109:227–241. <https://doi.org/10.1016/j.tws.2016.09.024>
11. Amraei M, Ahola A, Afkhami S et al (2019) Effects of heat input on the mechanical properties of butt-welded high and ultra-high strength steels. *Eng Struct* 198:109460. <https://doi.org/10.1016/j.engstruct.2019.109460>
12. Guo W, Li L, Dong S et al (2017) Comparison of microstructure and mechanical properties of ultra-narrow gap laser and gas-metal-arc welded S960 high strength steel. *Opt Lasers Eng* 91:1–15. <https://doi.org/10.1016/j.optlaseng.2016.11.011>
13. Gu W, Campbell J, Tang Y et al (2022) Indentation plastometry of welds. *Adv Eng Mater* 24:2101645. <https://doi.org/10.1002/adem.202101645>
14. Afkhami S, Javaheri V, Amraei M et al (2022) Thermomechanical simulation of the heat-affected zones in welded ultra-high strength steels: microstructure and mechanical properties. *Mater Des* 213:110336. <https://doi.org/10.1016/j.matdes.2021.110336>
15. Murakami Y (2019) *Metal fatigue: effects of small defects and nonmetallic inclusions*. 2nd Edition
16. Pavlina EJ, Van Tyne CJ (2008) Correlation of yield strength and tensile strength with hardness for steels. *J Mater Eng Perform* 17:888–893. <https://doi.org/10.1007/S11665-008-9225-5/FIGURES/8>
17. Tong L, Niu L, Jing S et al (2018) Low temperature impact toughness of high strength structural steel. *Thin-Walled Struct* 132:410–420. <https://doi.org/10.1016/j.tws.2018.09.009>
18. Sutton MA, Yan JH, Avril S et al (2008) Identification of heterogeneous constitutive parameters in a welded specimen: uniform stress and virtual fields methods for material property estimation. *Exp Mech* 48:451–464. <https://doi.org/10.1007/s11340-008-9132-6>
19. Yan R, Mela K, Yang F et al (2023) Equivalent material properties of the heat-affected zone in welded cold-formed rectangular hollow section connections. *Thin-Walled Struct* 184:110479. <https://doi.org/10.1016/j.tws.2022.110479>
20. Yan R, Xin H, Yang F et al (2022) A method for determining the constitutive model of the heat-affected zone using digital image correlation. *Constr Build Mater* 342:127981. <https://doi.org/10.1016/j.conbuildmat.2022.127981>
21. Rodrigues DM, Menezes LF, Loureiro A, Fernandes JV (2004) Numerical study of the plastic behaviour in tension of welds in high strength steels. *Int J Plast* 20:1–18. [https://doi.org/10.1016/S0749-6419\(02\)00112-2](https://doi.org/10.1016/S0749-6419(02)00112-2)
22. Hollomon JH (1945) Tensile deformation. *Aime Trans* 12(162):268–290
23. Swift HW (1952) Plastic instability under plane stress. *J Mech Phys Solids* 1:1–18. [https://doi.org/10.1016/0022-5096\(52\)90002-1](https://doi.org/10.1016/0022-5096(52)90002-1)
24. Voce E (1948) The relationship between stress and strain for homogeneous deformations. *J Inst Met* 74:537–562
25. Kocks UF, Mecking H (2003) Physics and phenomenology of strain hardening: the FCC case. *Prog Mater Sci* 48:171–273. [https://doi.org/10.1016/S0079-6425\(02\)00003-8](https://doi.org/10.1016/S0079-6425(02)00003-8)
26. Choudhary BK, Christopher J, Samuel EI (2012) Applicability of Kocks-Mecking approach for tensile work hardening in P9 steel. *Mater Sci Technol* 28:644–650. <https://doi.org/10.1179/1743284711Y.0000000106>
27. Choudhary BK, Rao Palaparti DP (2012) Comparative tensile flow and work hardening behaviour of thin section and forged thick section 9. J Nucl Mater 430:72–81. <https://doi.org/10.1016/j.jnucmat.2012.06.046>
28. Amraei M, Afkhami S, Javaheri V et al (2020) Mechanical properties and microstructural evaluation of the heat-affected zone in ultra-high strength steels. *Thin-Walled Struct* 157:107072. <https://doi.org/10.1016/j.tws.2020.107072>
29. Schwab R, Harter A (2021) Extracting true stresses and strains from nominal stresses and strains in tensile testing. *Strain* 57:e12396. <https://doi.org/10.1111/str.12396>
30. Ludwik P (1909) *Elemente der technologischen Mechanik*. Springer
31. Ludwigson DC (1971) Modified stress-strain relation for FCC metals and alloys. *Metall Trans* 2:2825–2828. <https://doi.org/10.1007/BF02813258>
32. Mondal C, Podder B, Ramesh Kumar K, Yadav DR (2014) Constitutive description of tensile flow behavior of cold flow-formed AFNOR 15CDV6 steel at different deformation levels. *J Mater Eng Perform* 23:3586–3599. <https://doi.org/10.1007/s11665-014-1127-0>
33. Mondal C, Singh AK, Mukhopadhyay AK, Chattopadhyay K (2013) Tensile flow and work hardening behavior of hot cross-rolled AA7010 aluminum alloy sheets. *Mater Sci Eng, A* 577:87–100. <https://doi.org/10.1016/j.msea.2013.03.079>
34. Mazaheri Y, Jahanara AH, Sheikhi M, Kalashami AG (2019) High strength-elongation balance in ultrafine grained ferrite-martensite dual phase steels developed by thermomechanical processing. *Mater Sci Eng, A* 761:138021. <https://doi.org/10.1016/j.msea.2019.06.031>
35. Samuel EI, Paulose N, Nandagopal M et al (2019) Tensile deformation and work hardening behaviour of AISI 431 martensitic stainless steel at elevated temperatures. *High Temp Mater Processes (London)* 38:916–926. <https://doi.org/10.1515/htmp-2019-0028>
36. Choudhary BK, Christopher J, Rao Palaparti DP et al (2013) Influence of temperature and post weld heat treatment on tensile stress-strain and work hardening behaviour of modified 9Cr–1Mo steel. *Mater Des* 1980–2015(52):58–66. <https://doi.org/10.1016/j.matdes.2013.05.020>
37. Sainath G, Choudhary BK, Christopher J et al (2015) Applicability of Voce equation for tensile flow and work hardening behaviour of P92 ferritic steel. *Int J Press Vessels Pip* 132–133:1–9. <https://doi.org/10.1016/j.ijpvp.2015.05.004>
38. Bambach M, Sizova I, Bolz S, Weiß S (2016) Devising strain hardening models using Kocks-Mecking plots—a comparison of model development for titanium aluminides and case hardening steel. *Metals (Basel)* 6:204. <https://doi.org/10.3390/met6090204>
39. Soares GC, Gonzalez BM, de Arruda SL (2017) Strain hardening behavior and microstructural evolution during plastic deformation of dual phase, non-grain oriented electrical and AISI 304 steels. *Mater Sci Eng, A* 684:577–585. <https://doi.org/10.1016/j.msea.2016.12.094>
40. Vafaeian S, Fattah-alhosseini A, Mazaheri Y, Keshavarz MK (2016) On the study of tensile and strain hardening behavior of a thermomechanically treated ferritic stainless steel. *Mater Sci Eng, A* 669:480–489. <https://doi.org/10.1016/j.msea.2016.04.050>
41. Afkhami S, Javaheri V, Dabiri E et al (2022) Effects of manufacturing parameters, heat treatment, and machining on the physical and mechanical properties of 13Cr10Ni1.7Mo2Al0.4Mn0.4Si steel processed by laser powder bed fusion. *Mater Sci Eng, A* 832:142402. <https://doi.org/10.1016/j.msea.2021.142402>
42. Ghafouri M, Afkhami S, Pokka A-P et al (2024) Effect of temperature on the plastic flow and strain hardening of direct-quenched ultra-high strength steel S960MC. *Thin-Walled Struct* 194:111319. <https://doi.org/10.1016/j.tws.2023.111319>
43. Chowdhury SM, Chen DL, Bhole SD et al (2010) Tensile properties and strain-hardening behavior of double-sided arc welded and friction stir welded AZ31B magnesium alloy. *Mater Sci Eng, A* 527:2951–2961. <https://doi.org/10.1016/j.msea.2010.01.031>
44. Luo J, Mei Z, Tian W, Wang Z (2006) Diminishing of work hardening in electroformed polycrystalline copper with nano-sized and

- uf-sized twins. Mater Sci Eng, A 441:282–290. <https://doi.org/10.1016/J.MSEA.2006.08.051>
45. Mente T, Boellinghaus Th (2016) Numerical investigations on hydrogen-assisted cracking in duplex stainless steel microstructures. Cracking phenomena in welds IV. Springer International Publishing, Cham, pp 329–359
  46. Boellinghaus Th, Mente T, Wongpanya P et al (2016) Numerical modelling of hydrogen assisted cracking in steel welds. Cracking phenomena in welds IV. Springer International Publishing, Cham, pp 383–439

**Publisher's Note** Springer Nature remains neutral with regard to jurisdictional claims in published maps and institutional affiliations.